ISSN Number: 2454-2024(Online)

International Journal of Technical Research & Science

ANALYSIS OF HYBRID SOLAR - PV WIND STAND-ALONE SYSTEMS USING ARTIFICIAL INTELLIGENCE TECHNIQUES

Sunil, Deepak Kumar Joshi, Nirma Kumari Sharma
E-Mail Id: sunilyadav10july@gmail.com
Department of Electrical Engineering, Mewar University, Chittorgarh, Rajasthan, India

Abstract- This research proposes a solution to the challenges posed by the intermittent nature of renewable energy sources (RES) like wind and solar electricity through the utilization of a hybrid RES system, comprising a solar photovoltaic (PV) array and a wind turbine generator (WTG). The system's power delivery and quality are enhanced using AI technology, particularly neural networks employed in an innovative eye-based control technique. By integrating energy storage systems (ESS) and employing advanced AI-based control methods, the power quality of the hybrid RES system is significantly improved. This improvement, characterized by reduced voltage and frequency stress, enables the system to operate reliably across various weather conditions, thus ensuring consistent and dependable power supply. Standalone hybrid renewable energy systems, combining solar, wind, and energy storage devices, offer a viable solution for delivering safe and reliable power in rural areas. However, challenges such as voltage swings and harmonic distortion may arise due to the erratic nature of renewable energy sources. In this study, an AI-driven approach is proposed to address these challenges. The system predicts the output power of solar and wind systems using techniques like artificial neural networks (ANN) and fuzzy logic (FL), enabling the energy storage system to balance power generation and consumption based on anticipated values. This dynamic adjustment of output power to match load demand enhances power quality. To ensure the accuracy of prediction models and optimize system effectiveness, a real-time monitoring system is implemented. MATLAB/Simulink simulations validate the proposed approach, demonstrating significant improvements in power quality metrics such as total harmonic distortion (THD) reduction and power factor (PF) enhancement. Additionally, the proposed technique maintains a consistent power output across varying weather conditions, thereby enhancing system reliability.

Keywords: PV, WECS, Battery, ANN, FLC, ESS, standalone hybrid system.

1. INTRODUCTION

As global energy demand continues to rise and conventional energy sources diminish, the world increasingly looks towards renewable energy sources (RES) due to their widespread availability and environmental friendliness. India leads one of the largest renewable capacity expansion programs globally, with distributed energy generation systems, such as photovoltaic (PV) and wind energy, playing a pivotal role in clean energy production. However, the intermittent nature of solar and wind energy necessitates the integration of energy storage systems to ensure consistent energy supply, particularly in standalone applications. Hybrid renewable energy systems, combining multiple energy production sources, are gaining popularity to address this challenge. Wind and solar are the most commonly utilized RE systems, their installation locations carefully selected based on climate and topology considerations. The reliability of hybrid renewable energy systems is further enhanced by incorporating energy storage units, such as battery banks, to meet occasional load demands when renewable resource production is insufficient. These systems may operate connected or disconnected from the grid, with standalone systems entering islanding mode to prioritize power reliability. Despite their environmental benefits, RES integration poses challenges related to energy quality, particularly voltage and frequency stability issues. To address these challenges, this research proposes a unique AI-based system that harnesses solar and wind energy to power AI applications. By leveraging the complementary properties of solar and wind energy, the proposed system optimizes generation and utilization, thereby enhancing effectiveness and efficiency.

This study focuses on the conception, dynamic modeling, energy management, and control strategies of hybrid systems. The author proposes and examines an effective control strategy for managing energy in standalone hybrid solar-wind systems across various operational scenarios. Given the constant energy demand, the integration of batteries, supercapacitors, and backups into the hybrid system ensures its efficiency under fluctuating weather and load conditions.

2. PROPOSED CONFIGURATION AND MODELING OF THE HRES

The proposed Microgrid comprises a hybrid PV-Wind system integrated with a Hybrid Energy Storage System (HESS) to cater to the power needs of an off-grid community. The Microgrid includes a PV system connected via a boost (DC-DC) converter, a Wind Energy Conversion System (WECS) connected via a boost converter employing optimum torque (OT) based Maximum Power Point Tracking (MPPT) technique, and an HESS system connected via a bidirectional (DC-DC) converter controlled by an Artificial Neural Network (ANN) based

controller. These converters are linked to a common DC Link operating at 650 V. To power AC loads, a fuzzy-based Voltage Source Converter (VSC) controlled inverter is utilized. Additionally, a Dynamic Voltage Restorer (DVR) is connected at the Point of Common Coupling (PCC) to mitigate voltage sag/swell and improve system power quality. Any disparity between supply and load side feeders (F1 and F2 respectively) is rectified by injecting proper voltage via a voltage source inverter through an injecting transformer. An LC filter circuit is employed to suppress unwanted harmonic components. In scenarios where the generated wind and solar power exceed the load demand, the battery is charged initially. If the charging current of the battery surpasses a certain threshold, the supercapacitor is engaged in charging mode. Conversely, when the battery needs to discharge, and if the discharging current exceeds a set limit, the supercapacitor enters discharging mode to fulfill the load power demand.

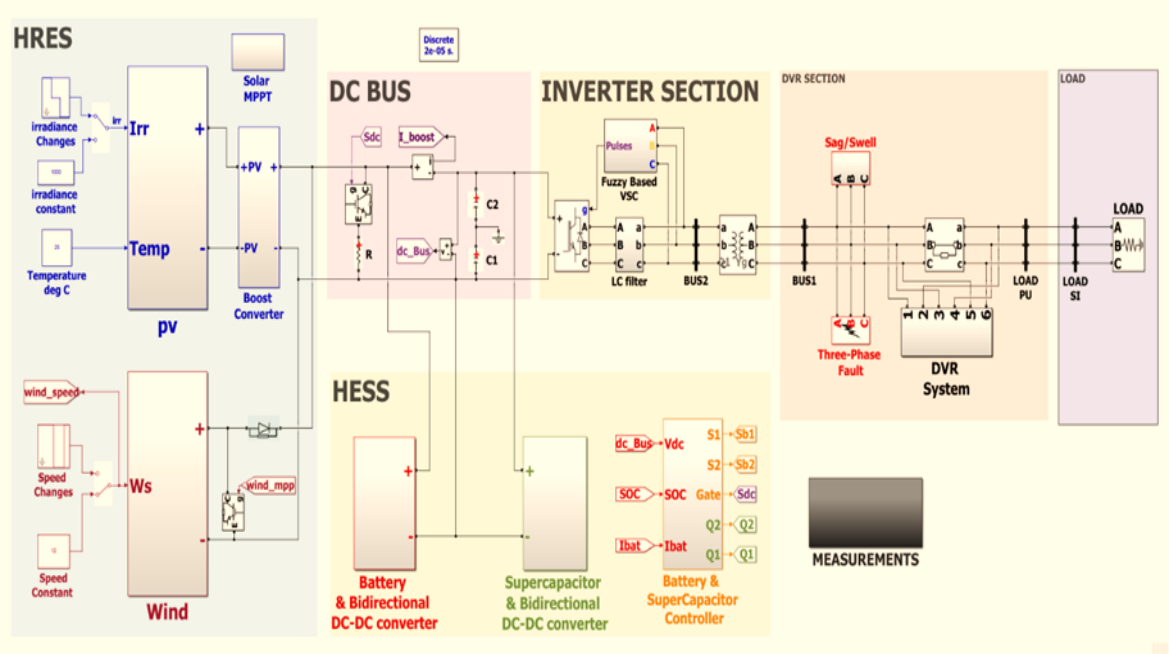

Fig. 2.1 MATLAB/Simulink Implementation of Dynamic Model for Hybrid Solar PV Wind Microgrid

2.1 PV System Modeling

The equivalent circuit of a PV cell is shown in Fig. 2.2 The current source I_{ph} represents the cell photocurrent. R_{sh} and R_s are the intrinsic shunt and series resistances of the cell, respectively. Usually the value of R_{sh} is very large and that of R_s is very small, hence they may be neglected to simplify the analysis. Practically, PV cells are grouped in larger units called PV modules and these modules are connected in series or parallel to create PV arrays which are used to generate electricity in PV generation systems. The equivalent circuit for PV array is shown in Fig. 2.3.

The voltage–current characteristic equation of a solar cell is provided:

Module photo-current I_{ph}: $I_{ph} = [\, I_{SC} + K_i\,(T - 298)] * I_r\,/1000$

Here: I_{ph}: photo-current (A), I_{sc}: short circuit current (A), K_i: short-circuit current of cell at 25 °C and 1000 W/m^2, T: operating temperature (K), I_r: solar irradiation (W/m2).

Module reverse saturation current I_{rs}: $I_{rs} = I_{sc}\,/[\exp\,(qV_{oc}\,/N_S\,knT) - 1]$

Here: q: electron charge = 1.6 × 10−19C, V_{oc}: open circuit voltage (V), Ns: number of cells connected in series, n: the ideality factor of the diode, k: Boltzmann's constant, = 1.3805 × 10−23 J/K.

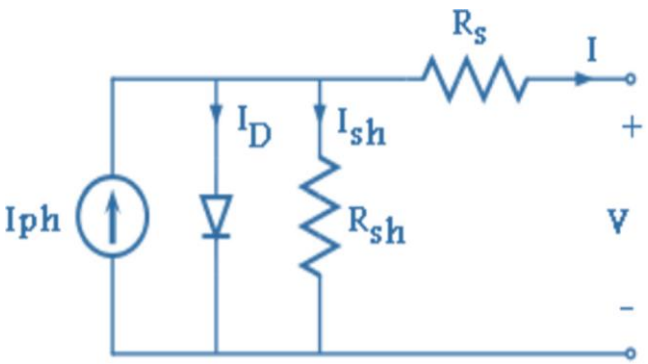

Fig. 2.2 PV Cell Equivalent Circuit

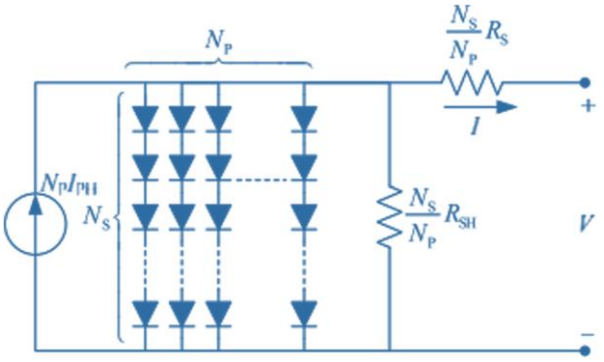

Fig. 2.3 Equivalent Circuit of Solar Array

The module saturation current I_0 varies with the cell temperature, which is given by:

$$I_0 = I_{rs}\left[\frac{T}{T_r}\right]^3 \exp\left[\frac{q \times E_{g0}}{nk}\left(\frac{1}{T} - \frac{1}{T_r}\right)\right] \quad (1)$$

Here: T_r: nominal temperature = 298.15 K, E_{g0}: band gap energy of the semiconductor = 1.1 eV The current output of PV module is:

$$I = N_P \times I_{ph} - N_P \times I_0 \times \left[\exp\left(\frac{V/N_S + I \times R_S/N_P}{n \times V_t}\right) - 1\right] - I_{sh} \quad (2)$$

With $V_t = \frac{k \times T}{q}$ and $I_{sh} = \frac{V \times N_P/N_S + I \times R_S}{R_{sh}}$

Here: Np: number of PV modules connected in parallel, R_s: series resistance (Ω), R_{sh}: shunt resistance (Ω), V_t: diode thermal voltage (V).

2.2 Wind System Modeling

The torque controller aims to enhance the efficiency of wind energy capture across a broad spectrum of wind speeds by ensuring the generated power remains at its optimum level. This is achieved through the block diagram depicted in Fig. 2.4. Irrespective of the wind velocity, the Maximum Power Point Tracking (MPPT) tool imposes a torque reference capable of extracting the maximum available power. The curve T_opt is represented as:

$$T_{opt} = K_{opt} * \omega_{opt}^2 \quad (3)$$

Where

$$K_{opt} = 0.5 * \rho A * \left(\frac{r_m}{\lambda_{opt}}\right)^3 * C_{P-max} \quad (4)$$

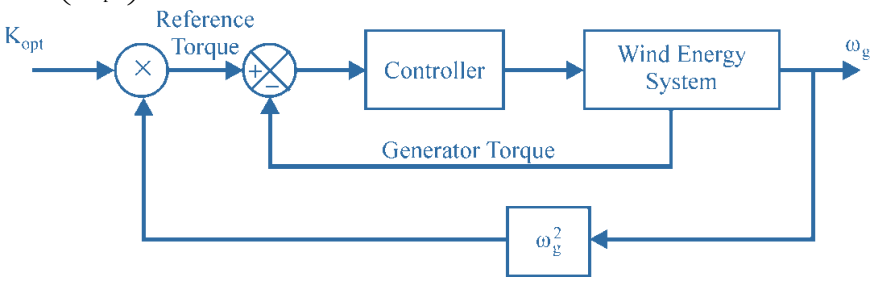

Fig. 2.4 Optimal Torque Control MPPT Method

The PMSG model is presented in figure. This dynamic model assumes no saturation, a sinusoidal back e.m.f. and negligible eddy current and hysteresis losses. It takes into account the iron losses and the dynamic equations for the PMSG currents are:

$$\frac{di_{md}}{dt} = \frac{1}{L_d}(v_d - R_{st} i_d + \omega L_q i_{mq}), \quad (5)$$

$$\frac{di_{mq}}{dt} = \frac{1}{L_d}(v_q - R_{st} i_q + \omega L_q i_{md} - \omega \psi_{PM}), \quad (6)$$

$$i_d = \frac{1}{R_c}(L_d \frac{di_{md}}{dt} - \omega L_q i_{mq} + R_c i_{md}), \quad (7)$$

$$i_q = \frac{1}{R_c}(L_q \frac{di_{mq}}{dt} + \omega L_d i_{md} + \omega \psi_{PM} + R_c i_{mq}), \quad (8)$$

$$i_{cd} = i_d - i_{md}, \quad (9)$$

$$i_{cq} = i_q - i_{mq}, \quad (10)$$

where i_d, i_q are the d_q axes currents, V'_d, V_q are the d_q axes voltages, i'_{cd}, i_{cq} are the d_q axes iron losses currents, i_{md}, i_{mq} are the d_q axes magnetizing currents, L_d, L_q are the d_q axes inductances, If/PM is the mutual flux due to magnets, OJ is the fundamental frequency of the stator currents, R_c is the iron losses resistance and R_{st} is the stator resistance.

The electromagnetic torque equation of the PMSG is: $T_e = \frac{2}{3} p\left[\psi_{PM} i_{mq} + (L_d - L_q) i_{md} i_{mq}\right]$ (11)

where p is the number of pole pairs

2.3 Modeling of Batteries

The Battery block implements a basic dynamic model parameterized to be best common types of rechargeable batteries.

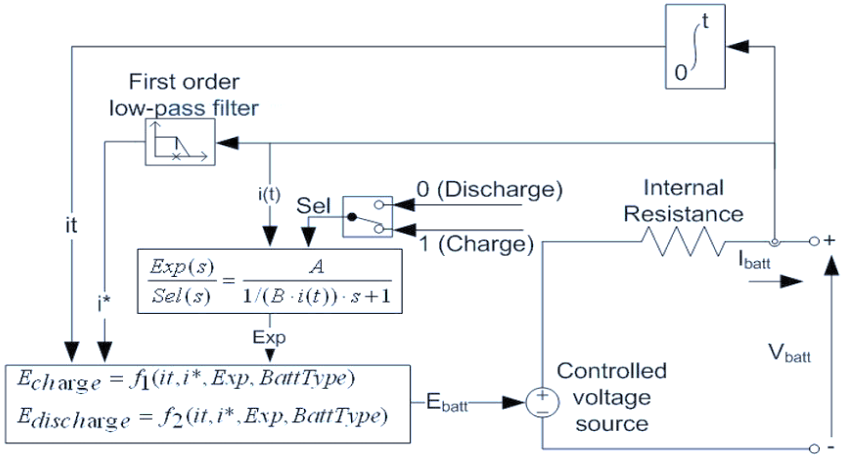

Fig. 2.5 Battery Equivalent Circuit

For the nickel-cadmium and nickel-metal-hydride battery types, the model uses these equations:

Discharge Model (i* > 0) $f_1(it, i*, i, Exp) = E_0 - K.\frac{Q}{Q - it}.i* - K.\frac{Q}{Q - it}.it + Laplace^{-1}\left(\frac{Exp(s)}{Sel(s)}.0\right)$

Charge Model (i* < 0) $f_2(it, i*, i, Exp) = E_0 - K.\frac{Q}{|it| + 0.1.Q}.i* - K.\frac{Q}{Q - it}.it + Laplace^{-1}\left(\frac{Exp(s)}{Sel(s)}.\frac{1}{s}\right)$.

In the equations:

Here, E_{Batt} is nonlinear voltage, in V, E_0 is constant voltage, in V, Exp(s) is exponential zone dynamics, in V, Sel(s) represents the battery mode, Sel(s) = 0 during battery discharge, Sel(s) = 1 during battery charging, K is polarization constant, in Ah^{-1}, i* is low frequency current dynamics, in A, i is battery current, in A.

it is extracted capacity, in Ah. Q is maximum battery capacity, in Ah., A is exponential voltage, in V., B is exponential capacity, in Ah^{-1}.

2.4 Supercapacitor Control Strategy

The role of supercapacitor Control Strategy is very important to make DC bus voltage constant and to remove the stress of the battery during pulsed load. The main focus of the proposed control scheme is on the supercapacitor reference ($i_{sc,ref}$) current generation which depends on the battery reference ($i_{B,ref}$) and battery error current (i_{error}). The current control of the supercapacitor is achieved by the control variable (D_{sc}). In proposed control scheme supercapacitor quickly responds towards the sudden change occurs in DC bus voltage due to environmental change or load variation. Fig. 2.6 shows the control strategy for supercapacitor.

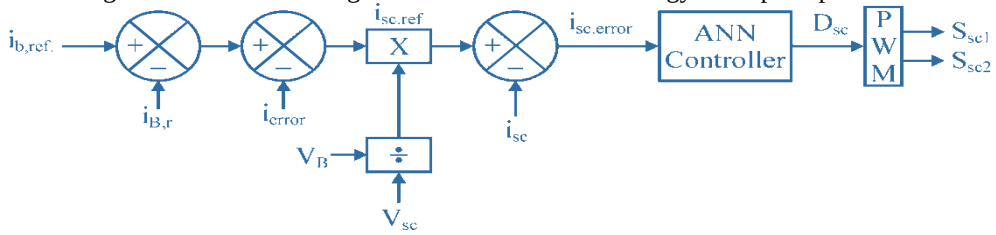

Fig. 2.6 Control Strategy for Supercapacitor

$$i_{sc,ref} = \left[i_{B,ref} - i_{B,r} + i_{error}\right]\frac{V_B}{V_{sc}} \quad (12)$$

The supercapacitor reference current ($i_{sc,ref}$) is obtained from battery reference current ($i_{B,ref}$) and the gain of DC

bus voltage estimator (G_{cv}) is given by equation.

$$i_{sc,ref} = \left[i_{B,ref} - \frac{2}{T}\int_{t_0}^{t_0+T} i_{B,ref}\,dt + i_B \right] \frac{V_B}{V_{sc}} \tag{13}$$

$$i_{sc,error} = \left[i_{B,ref} - \frac{2}{T}\int_{t_0}^{t_0+T} i_{B,ref}\,dt + i_B \right] \frac{V_B}{V_{sc}} - i_{sc} \tag{14}$$

$$i_{sc} = i_{B,ref}\frac{V_B}{V_{sc}} - \frac{2V_B}{TV_{sc}}\int_{t_0}^{t_0+T} i_{B,ref}\,dt + \frac{V_B}{V_{sc}} i_B - i_{sc,error} \tag{15}$$

The supercapacitor state model during boost mode operation is given by:

$$v_{sc} = L_{sc}\frac{di_{sc}}{dt} + v_{dc}\left(1 - D_{sc}\right) \tag{16}$$

$$c_{sc}\frac{dv_{dc}}{dt} = i_{sc}\left(1 - D_{sc}\right) + \frac{v_{dc}}{R, L_{eq}} \tag{17}$$

$$i_{sc} = i_{sc}D_{sc} + c_{sc}\frac{dv_{dc}}{dt} - \frac{v_{dc}}{R, L_{eq}} \tag{18}$$

By solving 3.63 and 3.64, the control variable D_{sc} is obtained

$$D_{sc} = \frac{v_B}{i_{sc}v_{sc}}\left[i_{B,ref} - \frac{2}{T}\int_{t_0}^{t_0+T} i_{B,ref}\,dt + i_B \right] - \frac{i_{sc,error}}{i_{sc}} - \frac{c_{sc}dv_{dc}}{i_{sc}dt} + \frac{v_{dc}}{i_{sc}R_{Leq}} \tag{19}$$

Where R_{Leq} ,is the equivalent load resistance

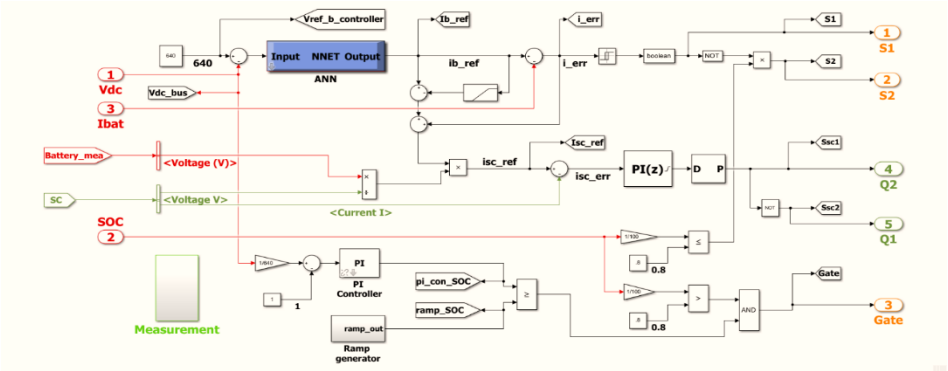

Fig. 2.7 Simulink Model of Novel Control Strategy

3. SIMULATION RESULTS AND DISCUSSION

Case-1: Simulation Response at Constant Irradiance (1000W/m²) and Constant Load (8kw) with Wind Speed Change (12 m/s to 8 m/s, 8 m/s to 10 m/s, 10 m/s to 12 m/s)

In this simulation test, both the Photovoltaic (PV) system and the Wind Energy Conversion System (WECS) operate simultaneously. The irradiation of the PV system is maintained constant at 1000 W/m², as depicted in Fig. 3.1 (a), throughout the test. Consequently, the power output of the PV system remains constant at 9.8 kW, as illustrated in Fig. 3.1 (b). Additionally, the load is kept constant at 8 kW, while the wind speed varies between 12 m/s to 8 m/s, 8 m/s to 10 m/s, and 10 m/s to 12 m/s, as shown in Fig. 3.2 (a). These variations in wind speed influence the performance of the WECS during the simulation test.

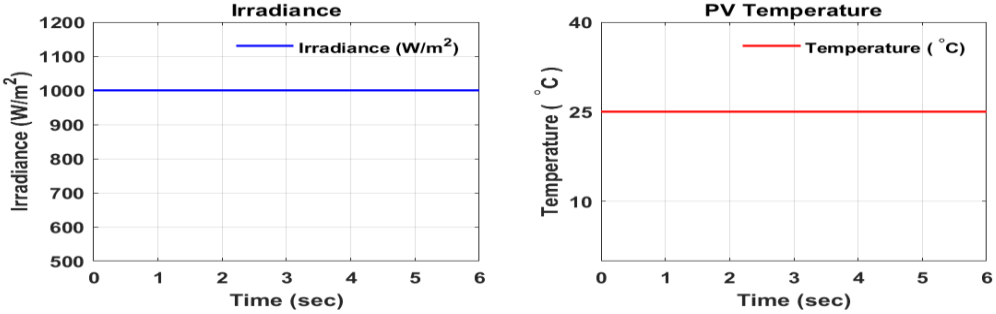

(a)

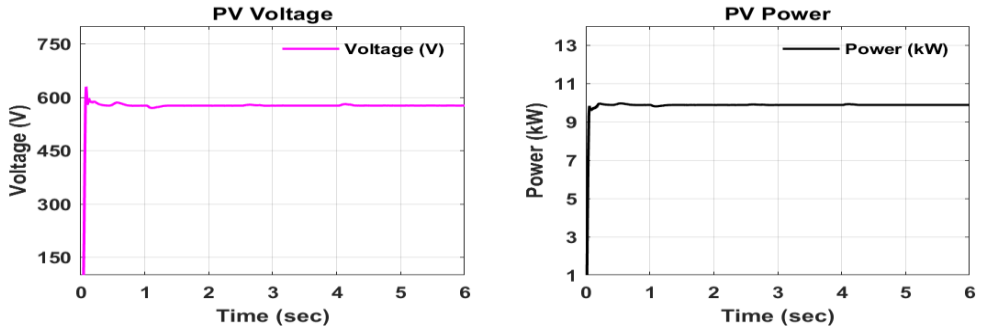

(b)

Fig. 3.1 Waveform of (a) Irradiance (W/m^2) and PV Temperature (°C), (b) PV Voltage (volt) and PV Output Power (kW)

The Fig. 3.1 shows the test results with constant irradiation at 1000 W/m^2. The Fig. 3.1 shows (a) Irradiance (W/m^2) and PV Temperature (°C), (b) PV Voltage (volt) and PV output power(kW).

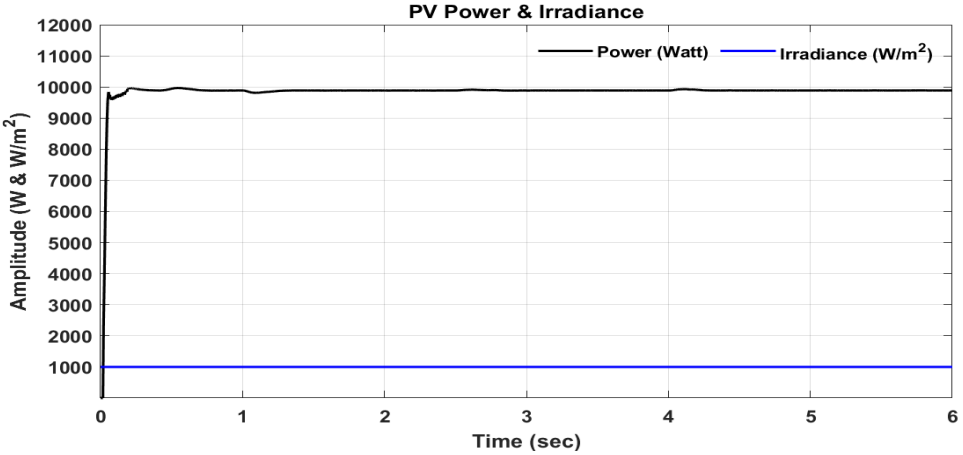

Fig. 3.2 PV System Output Power at Constant Irradiation 1000 W/m^2

From Fig. 3.2, it is clear that for constant irradiation 1000 W/m^2, the output power of the PV system is also remaining constant at 9.8 kw.

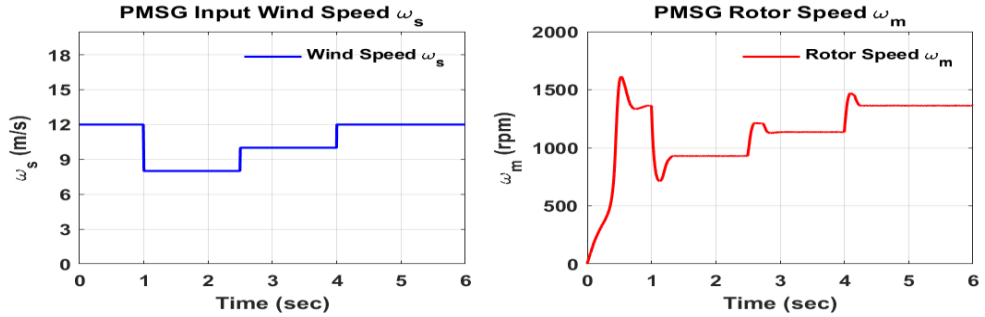

(a)

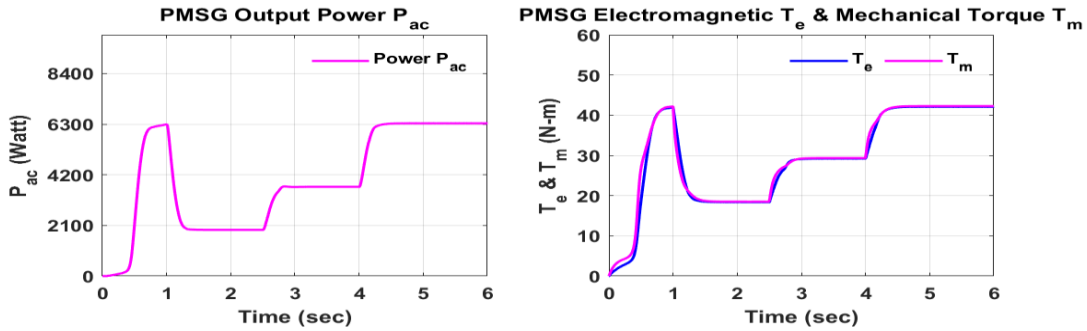

(b)

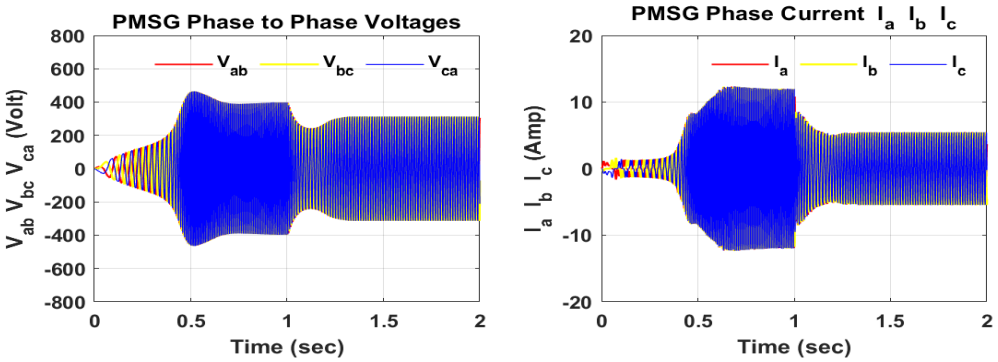

(c)

Fig. 3.3 Waveform of (a) Input Wind Speed ω_s and PMSG Speed ω_m, (b) PMSG Output Power P_{ac} and Electromagnetic & Mechanical Torque T_e & T_m, (c) PMSG Phase to Phase Voltages V_{ab} V_{bc} V_{ca}, (f) PMSG Phase Current I_a I_b Ic

The simulation results of the Wind Energy Conversion System (WECS) during varying wind speed are presented in Figure 3.3, showcasing: (a) The input wind speed (ωs) and PMSG speed (ωm). (b) PMSG output power (Pac) alongside electromagnetic and mechanical torque (Te & Tm). (c) PMSG phase-to-phase voltages (Vab, Vbc, Vca) and phase current (Ia, Ib, Ic). Analysis of the results reveals the following: At t = 0 sec to t = 1 sec, the input wind speed of the WECS is 12 m/s, resulting in a rotor speed of the PMSG at 1400 rpm. Correspondingly, the power output and torque are measured at 6.3 kW and 42 N-m, respectively. At t = 1 sec, the input wind speed of the WECS decreases to 8 m/s from 12 m/s, causing the rotor speed to decrease to 930 rpm. Consequently, the power output and torque decrease to 1.9 kW and 18.4 N-m, respectively. At t = 2.5 sec, the input wind speed of the WECS increases to 10 m/s from 8 m/s, resulting in the rotor speed increasing to 1132 rpm. Correspondingly, the power output and torque increase to 3.7 kW and 29.3 N-m, respectively. At t = 4 sec, the input wind speed of the WECS returns to 12 m/s, leading to the rotor speed reaching 1400 rpm again. Consequently, the power output and torque increase to 6.3 kW and 42 N-m, respectively. Fig. 3.4 illustrates the variation in the output power of the PMSG concerning the changed wind speed.

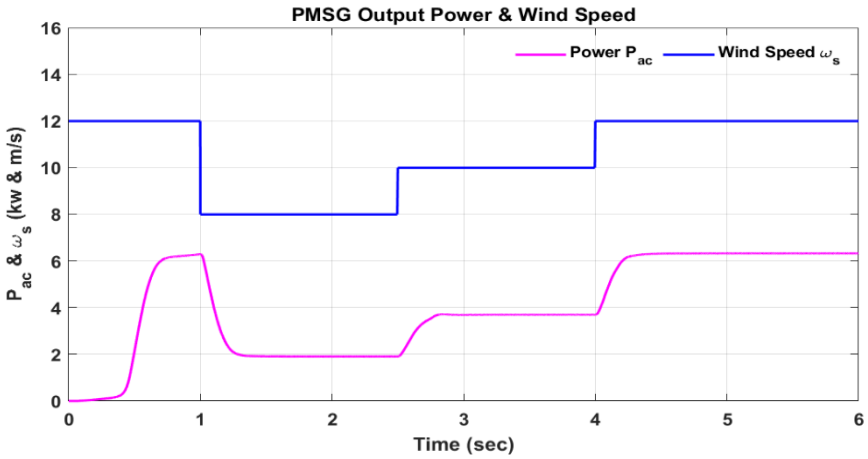

Fig. 3.4 Power Output When Wind Speed Changed from 12 m/s to 8 m/s, 8 m/s to 10 m/s, 10 m/s to 12 m/s

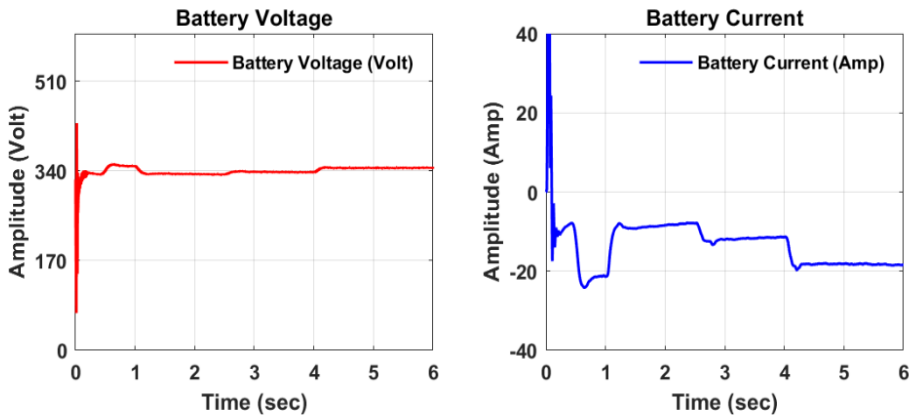

(a)

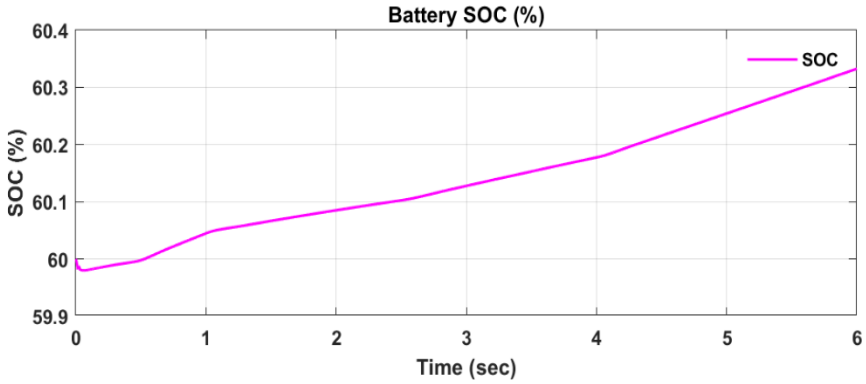

(b)

Fig. 3.5 Waveform of (a) Battery Output Voltage (volt) and Battery Output Current (Amp), (b) Battery SOC (%)

In this simulation, the power generated from the hybrid system is directed to the common DC bus. An Artificial Neural Network-based intelligent control strategy is employed to maintain a balance between generation and load power demand. Additionally, a hybrid storage system is integrated at the same DC bus via a DC-DC Buck-Boost converter.

The simulation results of the battery behavior during the test are depicted in Figure 3.5, comprising: (a) Battery voltage and battery current. (b) Battery State of Charge (SOC). In Figure 3.5 (a), it's observed that the battery voltage remains constant at 340V throughout the test. Initially, the SOC of the battery is set at 60%. At the simulation's onset, between time period t = 0 and t = 1 sec, when the irradiation for the PV system is 1000 W/m² and the wind speed of the WECS is 12 m/s, the combined output of the hybrid microgrid system amounts to 16.1 kW, surpassing the power demanded by the load. Consequently, surplus power is channeled to the battery through the DC-DC converter. The battery operates in the charging mode during this interval, with a charging current of 21.3 A, as indicated in Figure 3.5 (a). Simultaneously, the SOC of the battery begins to increase from its initial value, as shown in Figure 3.5 (b). At t = 1 sec, the wind speed of the WECS decreases to 8 m/s, while the irradiation for the PV system remains constant at 1000 W/m². Consequently, the power output of the WECS reduces to 1.9 kW. However, the combined output power of the hybrid microgrid during this period remains greater than the load power demand, amounting to 11.7 kW. The battery continues to charge, now with a reduced charging current of 9.5 A, leading to a slower rate of increase in SOC. Subsequently, at t = 2.5 sec, when the wind speed of the WECS increases to 10 m/s, the power output of the WECS rises to 3.7 kW, and the combined output power of the hybrid microgrid during this interval increases to 13.5 kW. The battery continues to charge with an increased charging current of approximately 12 A, with the rate of SOC increase also accelerating.

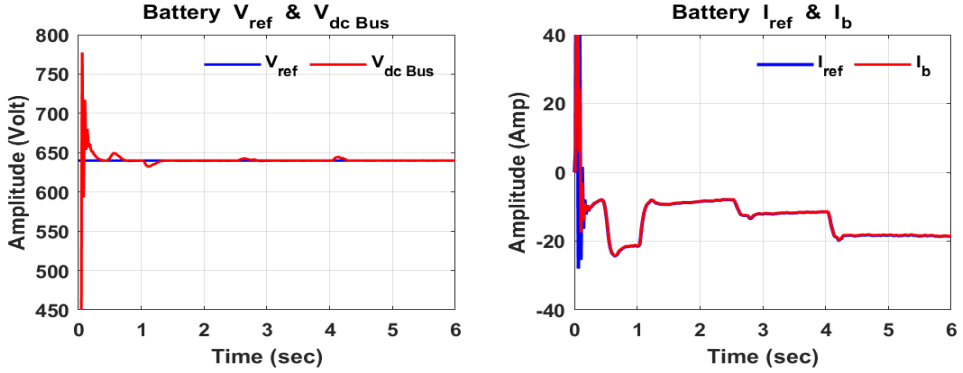

(a)

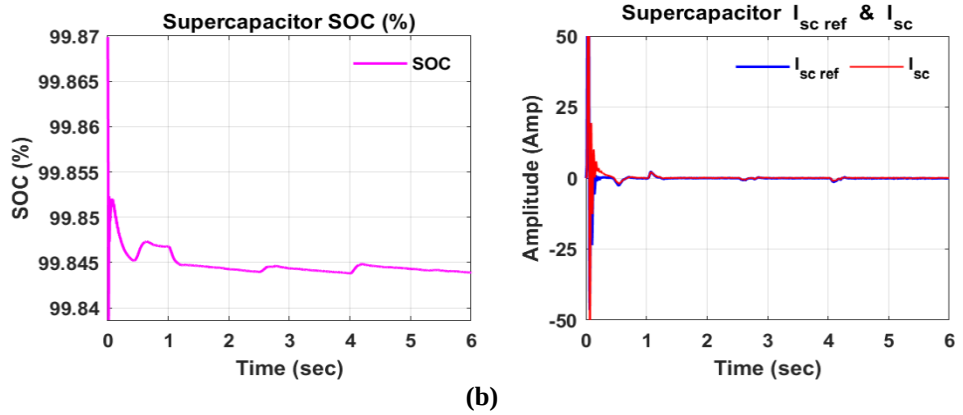

(b)

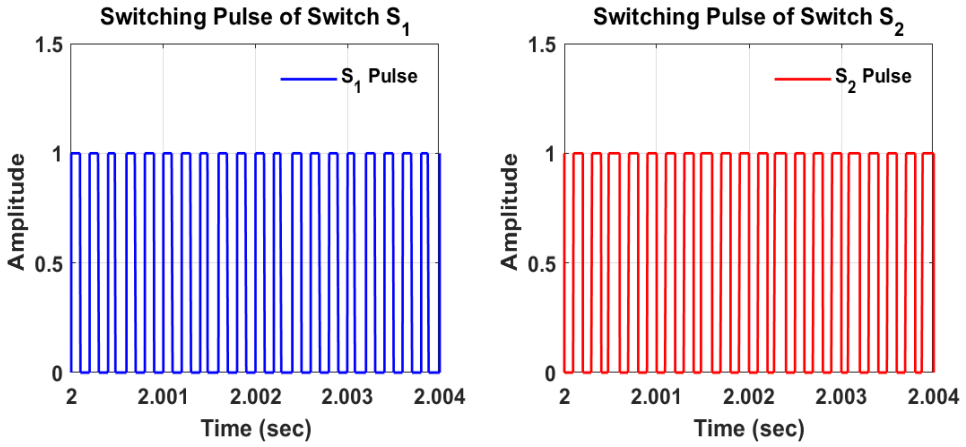

(c)

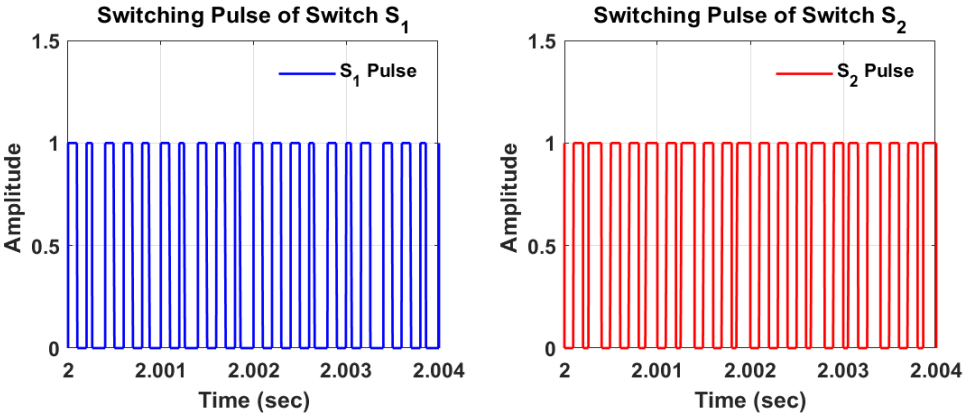

(d)

Fig. 3.6 Waveform of (a) Battery V_{ref} & V_{dcbus} (volt) and Battery I_{ref} & I_b (b) Supercapacitor I_{scref} & I_{sc} and Supercapacitor SOC (c) Battery switching Pulse of Switch S1 & S2, (d) Supercapacitor Switching Pulse of Switch S1 & S2

At t = 4 sec, the wind speed of the Wind Energy Conversion System (WECS) is further increased to 12 m/s, resulting in the power output of the WECS rising to 6.3 kW. Consequently, the combined output power of the hybrid microgrid during this interval reaches 16.1 kW. The battery charging current reaches 18.5 A, with the rate of rise of State of Charge (SOC) also increasing. The intelligent controller's strategy is designed to maintain the DC bus voltage constant, even when there are changes in the microgrid input. Figure 3.6 (a) illustrates the DC bus reference voltage alongside the actual DC bus voltage. It's evident from Figure 3.6 (a) that despite the changes in wind speed of the WECS in a stepped manner, the developed control strategy effectively maintains the actual DC bus voltage equal to the DC bus reference voltage. In Figures 3.7 (a) and (b), the battery reference current (Iref) and actual battery current (Ib), as well as the supercapacitor reference current (Isc ref) and actual supercapacitor current (Isc), alongside the supercapacitor SOC, are displayed, respectively. Additionally, the switching pulses of the DC-DC buck-boost converter switch S1 and S2 for the battery and supercapacitor are depicted in Figures 3.6 (c) and (d), respectively. The generated DC bus voltage is supplied to the fuzzy-controlled inverter, which generates AC output voltage for the load. Figure 3.7 illustrates the three-phase AC output voltage of the inverter, while Figure 3.8 showcases the switching pulse for the fuzzy-controlled inverter.

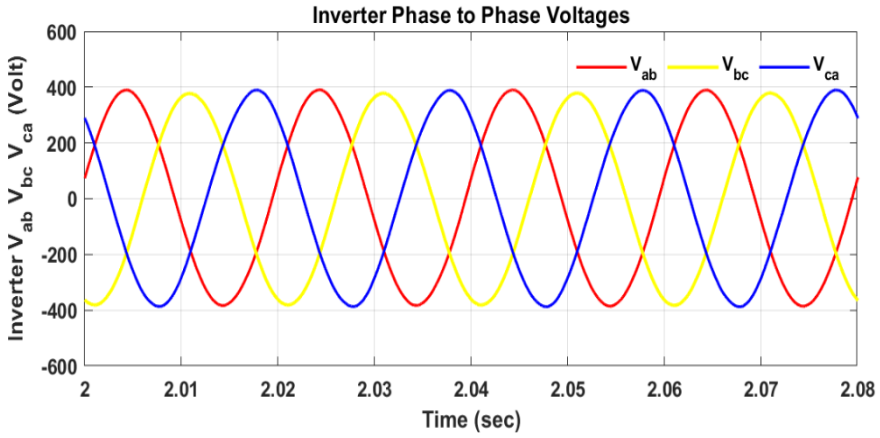

Fig. 3.7 Inverter Output Phase to Phase Voltages V_{ab}, V_{bc}, V_{ca}

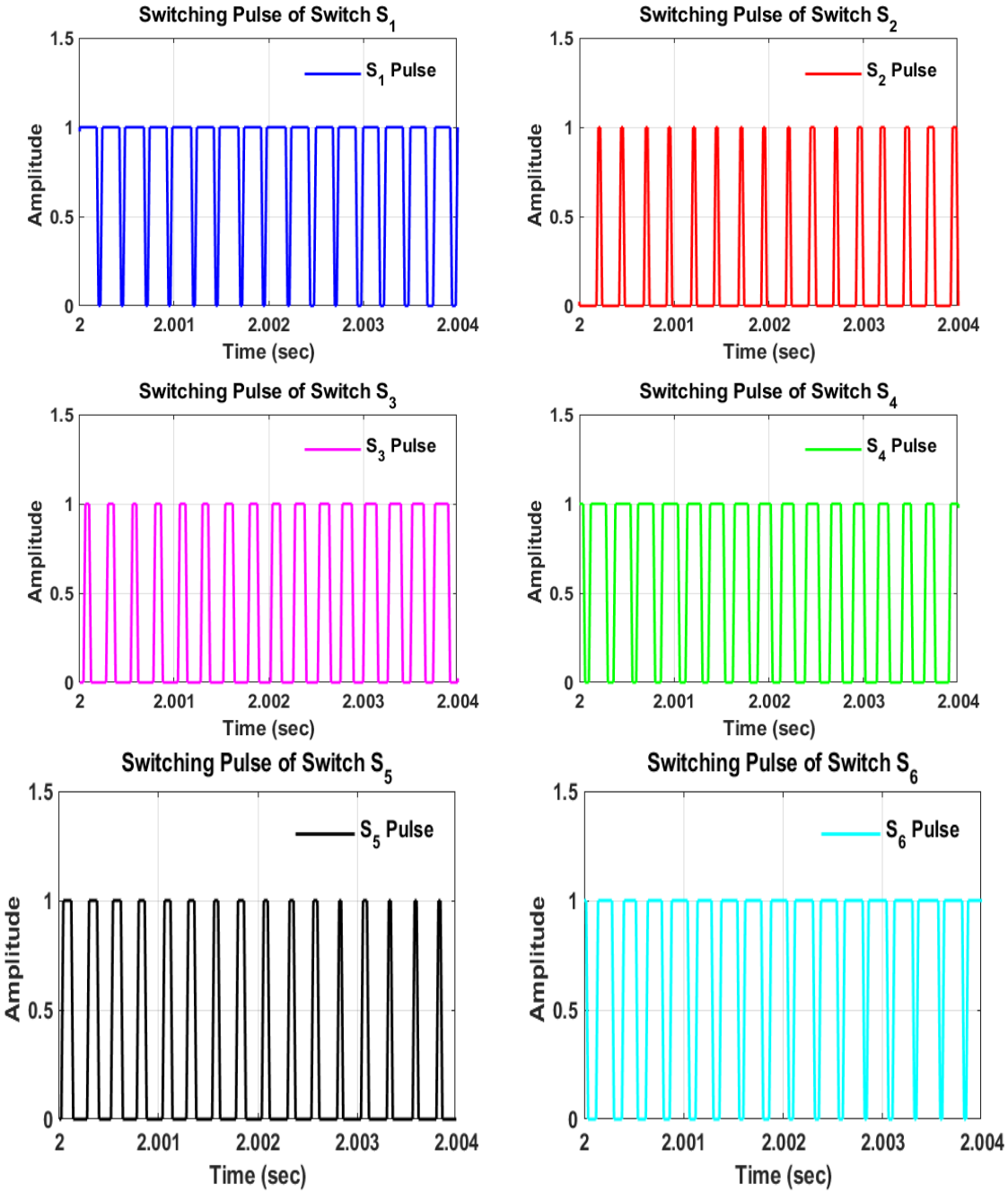

Fig. 3.8 Switching Pulses Waveform of Inverter Switches

During the test, a comparison of power between the load, battery system, Wind Energy Conversion System (WECS), Photovoltaic (PV) system, and supercapacitor is illustrated in Fig. 3.9. The load is maintained constant at 8 kW throughout the test, indicated by the black line. Since the irradiation remains constant at 1000 W/m² during the test, the power output of the PV system also remains constant at 9.8 kW, depicted by the blue line. However, the wind speed of the WECS varies in a stepped manner throughout the test, resulting in changes in the output power of the Permanent Magnet Synchronous Generator (PMSG). Specifically, from t = 1 sec to t = 2.5 sec, the wind speed decreases from 12 m/s to 8 m/s, causing the PMSG output power to decrease from 6.3 kW to 1.9 kW. Then, from t = 2.5 sec to t = 4 sec, the wind speed increases to 10 m/s from 8 m/s, leading to the PMSG output power increasing to 3.7 kW from 1.9 kW.

The power output of the Wind Energy Conversion System (WECS) is depicted by the magenta line. The red and green lines represent the power fed to the battery and supercapacitor, respectively. At time t = 4 sec and t = 6 sec, the power output of the Permanent Magnet Synchronous Generator (PMSG) is further increased to 6.3 kW because the wind speed has again reached 12 m/s. Consequently, the power fed to the battery also increases. Simultaneously, the supercapacitor enters charging mode to alleviate the current stress on the battery.

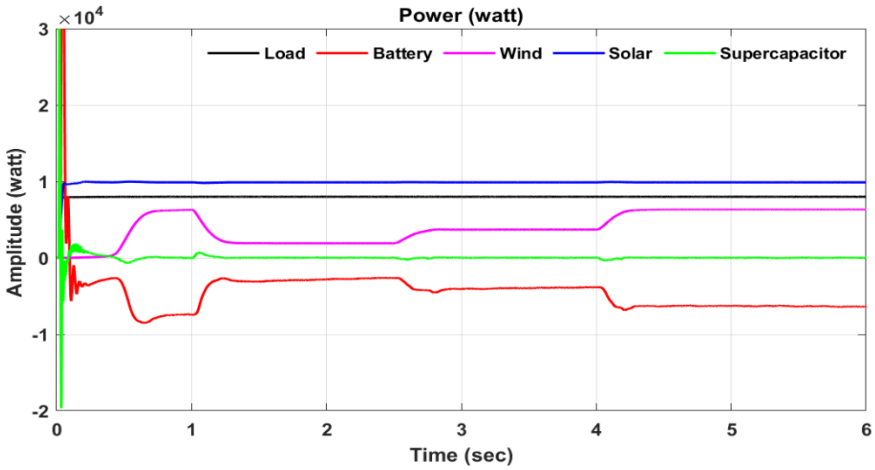

Fig. 3.9 Power Levels of Load, Battery, Wind, Solar System and Supercapacitor

CONCLUSION

The proposed maximum power point tracking techniques effectively extract optimum power solar wind renewable energy sources. The proposed intelligent control strategy effectively handled the hybrid energy storage system and maintain the DC bus voltage constant. The proposed intelligent control strategy successfully reduces the current stress of the battery by supercapacitor in both charging and discharging mode hence it improves the life of the battery. The power transfer in between hybrid energy storage system automatically handled by artificial neural network-based controller. The fuzzy based inverter restricts the voltage output at desired level and reduce the harmonics distortion within the range specified by IEEE 519 standard, hence improve the power quality. The simulation results show that both individual and hybrid generation system are capable of meeting the load requirements with hybrid energy storage system and keep the load voltage constant at specified limit during symmetrical and unsymmetrical operating conditions.

REFERENCES

[1] Imran Shafi; Harris Khan;Muhammad Siddique Farooq; Isabel de la Torre Diez; Yini Miró; Juan Castanedo Galán and Imran Ashraf 2023. "An Artificial Neural Network-Based Approach for Real-Time Hybrid Wind–Solar Resource Assessment and Power Estimation" Energies, Vol.16, issues no. 10, 2023.

[2] Satyajeet Sahoo et al. 2022. "Artificial Deep Neural Network in Hybrid PV System for Controlling the Power Management" Hindawi International Journal of Photoenergy, Vol.10, issues no. 02, 2022.

[3] Ahmed Aghmadi; Hossam Hussein; Osama A. Mohammed 2023. "Enhancing Energy Management System for a Hybrid Wind Solar Battery Based Standalone Microgrid" IEEE International Conference on Environment and Electrical Engineering held during 06-09 June 2023, pp. 1-6.

[4] P. Sai Sampath Kumar et al. 2023. "Energy Management System for Small Scale Hybrid Wind Solar Battery Based Microgrid" 4th International Conference on Design and Manufacturing Aspects for Sustainable Energy (ICMED-ICMPC 2023).

[5] Arul, P.G., Ramachandaramurthy, V.K. and Rajkumar, R. K., "Control strategies for a hybrid renewable energy system: A Review," Renewable and Sustainable Energy Reviews, vol. 42, pp. 597-608, 2015.

[6] Lazarov, V., Notton, G., Zarkov, Z. and Bochev, I. "Hybrid power systems with renewable energy sources types, structures, trends for research and development," In: Proceedings of 11th International conference on electrical machines, drives and power systems, held at Bulgaria during September 15-16, 2005, pp.515-520.

[7] Siddaiah, R. and Saini, R.P., "A review on planning, configurations, modeling and optimization techniques of hybrid renewable energy systems for off grid applications," Renewable and Sustainable Energy Reviews vol. 58, pp. 376-396, 2016.

[8] Chauhan, A. and Saini, R.P., "A review on Integrated Renewable Energy System based power generation for stand-alone applications: Configurations, storage options, sizing methodologies and control," Renewable and Sustainable Energy Reviews vol. 38, pp. 99-120, 2014.

[9] Nehrir, M. H., Wang, C., Strunz, H. Aki, Ramakumar, R., Bing, J., Miao, Z. and Salameh, "A review of hybrid renewable/alternative energy systems for electric power generation: configurations, control, and applications," IEEE Transactions on Sustainable Energy vol. 2, no.1, pp. 392-403, 2011.

[10] Wang, C. and Nehrir, M. H., "Power management of a stand-alone wind/photovoltaic/ fuel cell energy system," IEEE Transactions on energy conversion vol. 23, no. 5, pp. 957-967, 2008.

[11] M. Aarif; D. Joshi; R. Jangid and S.S. Sharma, "Grid Power Smoothing Management for Direct Drive PMSG Variable Speed Wind Energy Conversion System with Multilevel Converter", IEEE 7th International Conference on ICT for Sustainable Development, Organized by Global Knowledge Foundation during 29-30, July 2022 at Goa, India.

[12] Y. Joshi; J.k Maherchandani; V.K Yadav; R. Jangid; S. Vyas and S.S Sharma, "Performance Improvement of Standalone Battery Integrated Hybrid System" IEEE 7th International Conference on Electrical Energy Systems (ICEES), Organized by Sri Sivasubramaniya Nadar College of Engineering during 11-13 Feb. 2021at Chennai, India.
[13] R. Jangid; J.k Maherchandani; R.R. Joshi and B.D Vairagi, "Development of Advance Energy Management Strategy for Standalone Hybrid Wind & PV System Considering Rural Application", IEEE 2nd International Conference on Smart Systems and Inventive Technology, Organized by Francis Xavier Engineering College during November 27-29, 2019 at Tirunelveli, India.
[14] R. Jangid; K. Parikh and P. Anjana, "Reducing the Voltage Sag and Swell Problem in Distribution System Using Dynamic Voltage Restorer with PI Controller", International Journal of Soft Computing and Engineering, ISSN: 2231-2307, Vol.-3, Issue-6, January 2014.
[15] R. Jangid; J.k Maherchandani; V.K Yadav and R.K Swami, "Energy Management of Standalone Hybrid Wind-PV System", Journal of Intelligent Renewable Energy Systems (John Wiley & Sons, Inc.) Pages 179-198, 2022.
[16] H. Kumawat and R. Jangid, "Using AI Techniques to Improve the Power Quality of Standalone Hybrid Renewable Energy Systems", Crafting a Sustainable Future Through Education and Sustainable Development, IGI Global, Pages 219-228, 2023.
[17] H. Kumawat; R. Jangid, "Performance and Investigation of Two Drive Train Interfaced Permanent Magnet Synchronous Generator for Wind Energy Conversion System", Journal of Emerging Technologies and Innovative Research, ISSN:2349-5162, Volume 7, Issue 1, January 2020.
[18] R. Jangid et. al., "Smart Household Demand Response Scheduling with Renewable Energy Resources", IEEE Third International Conference on Intelligent Computing and Control System, Organized by Vaigai College of Engineering during May 15-17, 2019 at Madurai, India.
[19] S. Kumar; R. Jangid and K. Parikh "Comparative Performance Analysis of Adaptive Neuro-Fuzzy Inference System (ANFIS) & ANN Algorithms Based MPPT Energy Harvesting in Solar PV System." International Journal of Technical Research and Science, vol. 8, Issue 3, March 2023.
[20] S. Sharma; R. Jangid and K. Parikh "Development of Intelligent Control Strategy for Power Quality Improvement of Hybrid RES Using AI Technique" International Journal of Technical Research and Science, vol. VIII, Issue II, Feb. 2023.
[21] L. Jhala et al., "Development of Control Strategy for Power Management in Hybrid Renewable Energy System" International Journal of Technical Research and Science, vol. VI, Issue XII, Dec. 2021.
[22] Mohod, S.W. and Aware, M.V., "A STATCOM-control scheme for grid connected wind energy system for power quality improvement," IEEE Systems Journal vol. 4, no. 2, pp. 346-352, 2010.
[23] Frangieh, W. and Najjar, M. B., "Active control for power quality improvement in hybrid power systems," In: Proceedings of IEEE 3rd International Conference on Technological Advances in Electrical, Electronics and Computer Engineering held at Lebanon during April 29-30, 2015, pp. 218-223.
[24] Rini, T. H. and Razzak, M. A., "Voltage and power regulation in a solar-wind hybrid energy system," In: Proceedings of IEEE International WIE Conference on Electrical and Computer held at Dhaka during December 19-20, 2015, pp. 231-234.
[25] Prasad, V., "Voltage Compensation in a grid connected hybrid system using dynamic voltage restorer". In: Proceedings of IEEE International Conference on Power Instrumentation Control and Computing held at Thrissur during December 9-11, 2015, pp. 1-5.
[26] Jayasankar, V. N. and Vinatha, U., "Implementation of adaptive fuzzy controller in a grid connected wind-solar hybrid energy system with power quality improvement features," In: Proceedings of IEEE Biennial International Conference on Power and Energy Systems: Towards Sustainable Energy held at Bengaluru during January 21-23, 2016, pp. 1-5.